PAPER

Check for updates

Synthesis of trifluoromethylated aza-BODIPYs as fluorescence-^{19}F MRI dual imaging and photodynamic agents†

Anfeng Li,‡[a,b] Xingxing Peng,‡[a,b] Mou Jiang,‡[c] Tingjuan Wu,[a,b] Kexin Chen,[a,b] Zhigang Yang, [iD] [b] Shizhen Chen,[c] Xin Zhou, [iD] [c] Xing Zheng*[a] and Zhong-Xing Jiang [iD] *[b,c]

Dual-imaging agents with highly sensitive fluorescence (FL) imaging and highly selective fluorine-19 magnetic resonance imaging (^{19}F MRI) are valuable for biomedical research. At the same time, photosensitizers with a high reactive oxygen species (ROS) generating capability are crucial for photodynamic therapy (PDT) of cancer. Herein, a series of tetra-trifluoromethylated aza-boron dipyrromethenes (aza-BODIPYs) were conveniently synthesized from readily available building blocks and their physicochemical properties, including ultraviolet-visible (UV-Vis) absorption, FL emission, photothermal efficacy, ROS generating efficacy, and ^{19}F MRI sensitivity, were systematically investigated. An aza-BODIPY with 12 symmetrical fluorines was identified as a potent FL-^{19}F MRI dual-imaging traceable photodynamic agent. It was found that the selective introduction of trifluoromethyl (CF₃) groups into aza-BODIPYs may considerably improve their UV absorption, FL emission, photothermal efficacy, and ROS generating properties, which lays the foundation for the rational design of trifluoromethylated aza-BODIPYs in biomedical applications.

Introduction

Integrating multiple imaging modalities into a single agent provides accurate and comprehensive target information by taking advantage of every imaging technology,[1] while the integration of imaging and therapy capabilities into theranostics may significantly improve the therapeutic efficacy by utilizing real-time and personalized "drug–disease–therapy" information, *e.g.* imaging-guided drug therapy.[2] Among the imaging technologies, fluorescence imaging (FI) is the most used because of its convenience, high sensitivity and resolu-

[a]*Group of Lead Compound, Department of Pharmacy, Hunan Provincial Key Laboratory of Tumor Microenvironment Responsive Drug Research, Hunan Province Cooperative Innovation Center for Molecular Target New Drug Study, University of South China, Hengyang 421001, China. E-mail: zhengxing9166@sohu.com*
[b]*Hubei Province Engineering and Technology Research Center for Fluorinated Pharmaceuticals, School of Pharmaceutical Sciences, Wuhan University, Wuhan 430071, China. E-mail: zxjiang@whu.edu.cn*
[c]*State Key Laboratory of Magnetic Resonance and Atomic and Molecular Physics, National Center for Magnetic Resonance in Wuhan, Wuhan Institute of Physics and Mathematics, Innovative Academy of Precision Measurement Science and Technology, Chinese Academy of Sciences, Wuhan 430071, China*
†Electronic supplementary information (ESI) available: Synthetic procedures, photothermal and photodynamic measurements, and copies of the ¹H/¹³C/¹⁹F NMR and HRMS spectra of the compounds. See DOI: https://doi.org/10.1039/d2ob00297c
‡These authors contributed equally to this work.

tion. However, the tissue-depth limit of FI severely hampers its *in vivo* application. To this end, ^{19}F MRI perfectly complements FL by providing quantitative and highly selective "hotspot" images without ionizing radiation, tissue-depth limit, and background interference.[3] Therefore, integrating FI and ^{19}F MRI in a single agent enables sensitive *in vitro* studies on molecules, cells, and tissues with FL as well as selective and quantitative *in vivo* studies on animals and patients with ^{19}F MRI. Based on this idea, many FL-^{19}F MRI dual-imaging agents have been developed in recent years, which significantly promoted biomedical research.[4]

As a class of FL dyes with extraordinary FL, photothermal, and ROS generating capabilities, aza-BODIPYs have extensive application in medical imaging, photothermal therapy (PTT), and PDT.[5] Fluorination of aza-BODIPYs has been proven effective in improving the physicochemical properties and providing the ^{19}F MRI capability.[4d,6] However, these aza-BODIPYs suffer from either low ^{19}F MRI sensitivity due to low fluorine contents or limited availability due to complicated synthesis. Therefore, it is essential to develop novel aza-BODIPYs with high ^{19}F MRI sensitivity through convenient synthesis. Meanwhile, discovering fluorinated aza-BODIPYs with PTT and PDT capabilities may facilitate FL-^{19}F MRI-guided PTT/ PDT using just one agent to avoid the complex formulation, possible toxicity, and non-uniform pharmacokinetics of multiple agents. To address these issues, we herein designed a

This journal is © The Royal Society of Chemistry 2022

Org. Biomol. Chem., 2022, **20**, 3335–3341 | **3335**

Fig. 1 The structures of tetra-trifluoromethylated aza-BODIPYs **1a**, **1b**, **1d** and **1e**, and their non-trifluoromethylated counterparts **1c** and **1f**.

series of tetra-trifluoromethylated aza-BODIPYs as potential FL-^{19}F MRI dual imaging agents with their non-trifluoromethylated counterparts as references (Fig. 1). The introduction of four strong electron-withdrawing CF$_3$ groups on the peripheral phenyl rings would considerably rearrange the electron distribution of aza-BODIPYs, and therefore modify their physicochemical properties, such as UV absorption, FL emission, photothermal and photodynamic capabilities. To avoid the formation of isomers and simplify the synthesis, we designed aza-BODIPYs with four symmetrical CF$_3$ groups on the peripheral phenyl rings, which may also improve the ^{19}F MRI sensitivity by generating a uniform ^{19}F signal from twelve chemically equivalent fluorines (^{19}F). Moreover, the bulky size of CF$_3$ may relieve the aggregation-caused FL quenching (ACQ) of aza-BODIPYs, while the high lipophilicity of CF$_3$ may improve their pharmacokinetics.[7]

Experimental

General information

^{1}H, ^{13}C, and ^{19}F NMR spectra were recorded on a Bruker 400 MHz or 500 MHz. ^{1}H NMR spectra were referenced to tetramethylsilane (s, 0.00 ppm) using CDCl$_3$ as the solvent. ^{13}C NMR spectra were referenced to solvent carbons (77.16 ppm for CDCl$_3$, 67.21 ppm and 25.31 ppm for tetrahydrofuran-d_8). ^{19}F NMR spectra were referenced to 2% hexafluorobenzene (s, −164.90 ppm) in CDCl$_3$. The splitting patterns for ^{1}H NMR and ^{19}F NMR spectra were denoted as follows: s = singlet, d = doublet, t = triplet, q = quartet, dd = double doublet and m = multiplet. High-resolution mass spectra were recorded on a 4.7 Tesla FT-MS using Electrospray Ionization (ESI). Unless otherwise noted, solvents and reagents were purchased from commercial suppliers and used as received. Flash chromatography was performed on 200–300 mesh silica gel with ethyl acetate (EtOAc)/petroleum ether (PE, 60–90 °C) as the eluent. UV–Vis and fluorescence emission spectra were obtained using a UV-2600 UV–Vis spectrophotometer (Shimadzu, Japan) and an F-4700 spectrofluorophotometer (Hitachi, Japan), respectively.

A 660 nm laser was used for photothermal conversion and ROS generation experiments. ^{19}F MRI was performed on a 400 MHz Bruker BioSpec MRI system. The temperature of the magnet room was maintained at 24 °C during the entire MRI experiment. ^{19}F *in vitro* images were acquired using a gradient-echo (GRE) pulse sequence, method = RARE, matrix size = 32 × 32, SI = 20 mm, FOV = 3.0 cm, TR = 4000 ms, TE = 3 ms, scan time = 256 s.

General synthetic procedure

3-(3,5-Bis(trifluoromethyl)phenyl)-4-nitro-1-phenylbutan-1-one (5a). Compound **4a** (207.4 mg, 0.6 mmol), nitromethane (0.7 mL, 12.0 mmol) and NaOH (4.8 mg, 0.1 mmol) were dissolved in 5 mL of anhydrous EtOH and the mixture was refluxed for 12 h. The solution was cooled to room temperature, acidified with 2 N HCl, and extracted with EtOAc. The organic phase was dried with anhydrous Na$_2$SO$_4$ and evaporated in a vacuum to give the crude product, which was purified by flash chromatography to give compound **5a** (194.1 mg, yield 79%) as yellowish oil. ^{1}H NMR (400 MHz, CDCl$_3$) δ 7.92 (d, J = 7.2 Hz, 2H), 7.81 (s, 1H), 7.78 (s, 2H), 7.61 (t, J = 7.4 Hz, 1H), 7.48 (t, J = 7.7 Hz, 2H), 4.90 (dd, J = 13.1, 6.2 Hz, 1H), 4.75 (dd, J = 13.1, 8.4 Hz, 1H), 4.45–4.36 (m, 1H), 3.51 (dd, J = 6.9, 2.8 Hz, 2H). ^{19}F NMR (376 MHz, CDCl$_3$) δ −66.02 (s). ^{13}C NMR (101 MHz, CDCl$_3$) δ 195.9, 142.1, 135.9, 134.2, 132.4 (q, J = 33.5 Hz), 129.0, 128.1, 123.1 (q, J = 273.0 Hz), 122.4–122.1 (m), 78.7, 41.2, 38.9. HRMS (ESI) m/z: [M + Na]$^+$ calcd for C$_{18}$H$_{13}$F$_6$NO$_3^+$: 428.0692, found 428.0691.

1-(3,5-Bis(trifluoromethyl)phenyl)-4-nitro-3-phenylbutan-1-one (5b). **5b** was prepared as yellowish oil in 63% yield (8.5 g) from **4b** (5.0 g, 14.5 mmol) using the same procedure for **5a**, expect that the base was diethyl amine (7.5 ml, 71.6 mmol). ^{1}H NMR (400 MHz, CDCl$_3$) δ 8.32 (s, 2H), 8.07 (s, 1H), 7.39–7.32 (m, 2H), 7.32–7.26 (m, 3H), 4.82 (dd, J = 12.6, 7.3 Hz, 1H), 4.73 (dd, J = 12.6, 7.3 Hz, 1H), 4.30–4.20 (m, 1H), 3.53 (dd, J = 6.8, 2.6 Hz, 2H). ^{19}F NMR (376 MHz, CDCl$_3$) δ −66.12 (s). ^{13}C NMR (101 MHz, CDCl$_3$) δ 194.4, 138.5, 137.8, 132.6 (q, J = 34.2 Hz), 129.4, 128.3, 128.2 (d, J = 4.2 Hz), 127.6, 127.0–126.7 (m), 122.9 (q, J = 273.3 Hz), 110.1, 79.3, 41.9, 39.2. HRMS (ESI) m/z: [M + Na]$^+$ calcd for C$_{18}$H$_{13}$F$_6$NO$_3^+$: 428.0692, found 428.0690.

3-(3,5-Bis(trifluoromethyl)phenyl)-1-(4-methoxy phenyl)-4-nitrobutan-1-one (5d). **5d** was prepared as yellowish oil in 83% yield (4.8 g) from **4d** (5.0 g, 13.4 mmol) using the same procedure for **5a**. ^{1}H NMR (400 MHz, CDCl$_3$) δ 7.89 (d, J = 8.9 Hz, 2H), 7.79 (s, 1H), 7.78 (s, 2H), 6.93 (d, J = 8.9 Hz, 2H), 4.90 (dd, J = 13.1, 6.0 Hz, 1H), 4.74 (dd, J = 13.1, 8.6 Hz, 1H), 4.44–4.32 (m, 1H), 3.86 (s, 3H), 3.49–3.36 (m, 2H). ^{19}F NMR (376 MHz, CDCl$_3$) δ −65.90 (s). ^{13}C NMR (101 MHz, CDCl$_3$) δ 194.3, 164.3, 142.3, 132.4 (q, J = 33.4 Hz), 130.5, 129.0, 128.1, 127.2, 123.2 (q, J = 273.0 Hz), 122.2–122.0 (m), 114.1, 78.7, 55.7, 40.8, 39.0. HRMS (ESI) m/z: [M + Na]$^+$ calcd for C$_{19}$H$_{15}$F$_6$NO$_4^+$: 458.0797, found 458.0794.

1-(3,5-Bis(trifluoromethyl)phenyl)-3-(4-methoxy phenyl)-4-nitrobutan-1-one (5e). **5e** was prepared as yellowish oil in 77% yield (1.8 g) from **4e** (2.0 g, 4.5 mmol) using the same procedure for **5a**. ^{1}H NMR (400 MHz, CDCl$_3$) δ 8.33 (s, 2H), 8.07

3336 | *Org. Biomol. Chem.*, 2022, **20**, 3335–3341

This journal is © The Royal Society of Chemistry 2022

(s, 1H), 7.20 (d, *J* = 8.7 Hz, 2H), 6.85 (d, *J* = 8.7 Hz, 2H), 4.78 (dd, *J* = 12.5, 7.2 Hz, 1H), 4.67 (dd, *J* = 12.5, 7.5 Hz, 1H), 4.23–4.13 (m, 1H), 3.75 (s, 3H), 3.58–3.41 (m, 2H). ^{19}F NMR (376 MHz, CDCl$_3$) δ −66.14 (s). ^{13}C NMR (101 MHz, CDCl$_3$) δ 194.6, 159.3, 137.9, 132.5 (q, *J* = 34.0 Hz), 130.3, 128.6, 128.2(d, *J* = 3.7 Hz), 126.8–126.5 (m), 122.9 (q, *J* = 273.0 Hz), 114.6, 79.5, 55.3, 42.0, 38.5. HRMS (ESI) *m/z*: [M + Na]$^+$ calcd for C$_{19}$H$_{15}$F$_6$NO$_4^+$: 458.0797, found 458.0793.

BF$_2$ chelate of 3-(3,5-bis(trifluoromethyl)phenyl)-*N*-(3-(3,5-bis(trifluoromethyl)phenyl)-5-phenyl-1*H*-pyrrol-2-yl)-5-phenyl-2*H*-pyrrol-2-imine (1a). A mixture of **5a** (1.9 g, 4.7 mmol) and ammonium acetate (12.9 g, 167.9 mmol) in methanol (MeOH, 40 mL) was refluxed for 24 h. After being cooled to room temperature, the reaction mixture was filtered, and the residue was washed with MeOH and collected, which was used in the next step without further purification. Under an argon atmosphere, the intermediate mentioned above and diisopropylethylamine (DIPEA, 0.7 mL, 4.0 mmol) were dissolved in dried dichloromethane (DCM, 5 mL), and the resulting solution was stirred at room temperature for 20 min. Then the boron trifluoride diethyl etherate complex (BF$_3$·Et$_2$O, 0.7 mL, 5.6 mmol) was added, and the resulting solution was stirred at room temperature for 24 h. After quenching the reaction mixture with water, the organic layer was collected, and the aqueous layer was extracted with dichloromethane. The combined organic layers were dried over anhydrous Na$_2$SO$_4$ and concentrated under vacuum. The residue was purified by flash chromatography to give compound **1a** as a brown metal color solid (256.0 mg, yield 14%). ^{1}H NMR (400 MHz, CDCl$_3$) δ 8.25 (s, 4H), 8.08 (dd, *J* = 7.4, 2.1 Hz, 4H), 7.92 (s, 2H), 7.58–7.50 (m, 6H), 7.17 (s, 2H). ^{19}F NMR (376 MHz, CDCl$_3$) δ −66.34 (s), −135.17 (dd, *J* = 61.2, 30.4 Hz). ^{13}C NMR (214 MHz, THF-*d$_8$*) δ 161.1, 146.4, 141.6, 135.2, 132.6 (q, *J* = 33.4 Hz), 132.2, 131.7, 130.78, 130.0, 129.30, 124.2 (q, *J* = 272.7 Hz), 123.2, 122.9. HRMS (MALDI-TOF) *m/z*: [M]$^+$ calcd for C$_{36}$H$_{18}$BF$_{14}$N$_3^+$: 769.1370, found 769.1363.

BF$_2$ chelate of 3-(3,5-bis(trifluoromethyl) phenyl)-*N*-(3-(3,5-bis(trifluoromethyl)phenyl)-5-phenyl-1*H*-pyrrol-2-yl)-5-phenyl-2*H*-pyrrol-2-imine (1b). **1b** was prepared in 16% yield (465.2 mg) as a purple solid from **5b** (3.0 g, 7.4 mmol) using the same procedure for **1a**. ^{1}H NMR (400 MHz, CDCl$_3$) δ 8.54 (s, 4H), 8.08 (d, *J* = 3.5 Hz, 4H), 7.99 (s, 2H), 7.56–7.45 (m, 6H), 7.14 (s, 2H). ^{19}F NMR (376 MHz, CDCl$_3$) δ −66.38 (s), −133.59 (dd, *J* = 65.9, 32.9 Hz). ^{13}C NMR (126 MHz, THF-*d$_8$*) δ 157.4, 147.0, 146.5, 134.0, 132.7, 132.6 (q, *J* = 33.7 Hz), 130.9, 130.7, 130.3, 129.4, 124.9, 124.1 (q, *J* = 272.7 Hz), 120.6. HRMS (MALDI-TOF) *m/z*: [M]$^+$ calcd for C$_{36}$H$_{18}$BF$_{14}$N$_3^+$: 769.1370, found 769.1361.

BF$_2$ chelate of 3-(3,5-bis(trifluoromethyl)phenyl)-*N*-(3-(3,5-bis(trifluoromethyl)phenyl)-5-(4-methoxyphenyl)-1*H*-pyrrol-2-yl)-5-(4-methoxyphenyl)-2*H*-pyrrol-2-imine (1d). **1d** was prepared in 25% yield (251.3 mg) as a green metal color solid from **5d** (1.4 g, 3.1 mmol) using the same procedure for **1c**. ^{1}H NMR (500 MHz, CDCl$_3$) δ 8.24 (s, 4H), 8.13 (d, *J* = 8.7 Hz, 4H), 7.89 (s, 2H), 7.15 (s, 2H), 7.05 (d, *J* = 8.7 Hz, 4H), 3.92 (s, 6H). ^{19}F NMR (471 MHz, CDCl$_3$) δ −66.21 (s), −135.68 (dd, *J* = 62.8, 31.7

Hz). ^{13}C NMR (214 MHz, THF-*d$_8$*). δ 164.0, 159.6, 146.3, 140.5, 135.8, 133.2, 132.7 (q, *J* = 33.4 Hz), 130.0, 124.4 (q, *J* = 272.7 Hz), 124.3, 122.9, 122.3, 115.2, 55.9. HRMS (MALDI-TOF) *m/z*: [M]$^+$ calcd for C$_{38}$H$_{22}$BF$_{14}$N$_3$O$_2^+$: 829.1582, found 829.1576.

BF$_2$ chelate of 5-(3,5-bis(trifluoromethyl)phenyl)-*N*-(5-(3,5-bis(trifluoromethyl)phenyl)-3-(4-methoxyphenyl)-1*H*-pyrrol-2-yl)-3-(4-methoxyphenyl)-2*H*-pyrrol-2-imine (1e). **1e** was prepared in 16% yield (115.4 mg) as a blue solid from **5e** (729.8 mg, 1.7 mmol) using the same procedure for **1c**. ^{1}H NMR (400 MHz, CDCl$_3$) δ 8.52 (s, 4H), 8.09 (d, *J* = 8.9 Hz, 4H), 7.96 (s, 2H), 7.02 (d, *J* = 9.1 Hz, 6H), 3.92 (s, 6H). ^{19}F NMR (376 MHz, CDCl$_3$) δ −66.24 (s), −132.78 (dd, *J* = 64.2, 31.9 Hz). ^{13}C NMR (126 MHz, CDCl$_3$) δ 160.9, 155.0, 145.2, 144.8, 132.4, 131.3 (q, *J* = 33.9 Hz), 130.5, 128.6, 123.9, 123.1, 122.8 (q, *J* = 273.0 Hz), 116.0, 113.7, 54.7. HRMS (MALDI-TOF) *m/z*: [M]$^+$ calcd for C$_{38}$H$_{22}$BF$_{14}$N$_3$O$_2^+$: 829.1582, found 829.1579.

Results and discussion

The synthesis was started with the condensation of acetophenones **2a**–**2c** and benzaldehydes **3a**–**3c** (Scheme 1). Initially, many attempts on the Claisen–Schmidt condensation of acetophenone **2a** and di-trifluoromethylated benzaldehyde **3b** failed to deliver enone **4a**, while a complex mixture was obtained. It was later found that because of the strong electron-withdrawing ability of two CF$_3$ groups, the high reactivity of benzaldehyde **3b** and the low stability of enone **4a** led to severe side reactions under the given conditions. Then the reaction time was shortened to 25 min by quenching the reaction with 2N HCl solution, which delivered enone **4a** in 76% yield. Later, similar issues were observed during the condensation of di-trifluoromethylated acetophenone **2b** and benzaldehyde **3a**, which were addressed by further shortening the reaction time
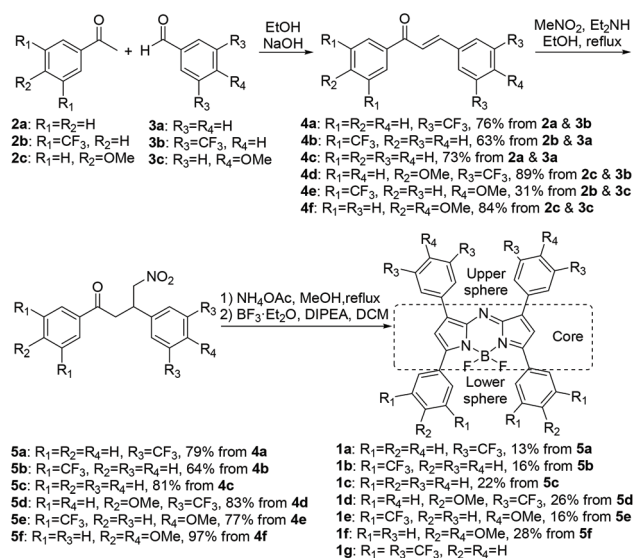
Scheme 1 Synthesis of trifluoromethylated aza-BODIPYs **1a**, **1b**, **1d** and **1e**, and their non-trifluoromethylated counterparts **1c** and **1f**.

This journal is © The Royal Society of Chemistry 2022

Org. Biomol. Chem., 2022, **20**, 3335–3341 | **3337**

to 8 min to obtain **4b** in 63% yield. However, extended reaction times were required to promote the dehydration of the intermediates for enones **4c**, **4d**, and **4f** with higher electron densities.[8] Next, Michael addition of the enones **4a–4f** with nitromethane under basic conditions provided ketones **5a–5f** in good yields.[9] Finally, condensation of ketones **5a–5f** and subsequently complexation with $BF_3 \cdot Et_2O$ gave aza-BODIPYs **1a–1e**, during which the condensation intermediates were not purified and directly used in the next step due to their poor stability and solubility.[10] Notably, many attempts to synthesize octa-trifluoromethylated aza-BODIPY **1g** were unsuccessful due to the low stability of the highly trifluoromethylated synthetic intermediates. The aza-BODIPYs and their intermediates were fully characterized using $^1H/^{13}C/^{19}F$ NMR and high-resolution mass spectra, which confirmed their chemical structures.

With aza-BODIPYs **1a–1f** in hand, their UV absorption and FL emission were then investigated. First, all the aza-BODIPYs except for **1e** showed a strong absorption peak in their UV-Vis spectra, respectively (Fig. 2a and Table 1). Aza-BODIPYs **1a–1c** had maximum absorption peaks between 644 and 656 nm. In comparison, aza-BODIPYs **1d–1f** with electron-donating methoxyl (MeO) groups gave much red-shifted maximum absorption peaks between 674 and 706 nm, respectively. Second, all the aza-BODIPYs except for **1e** gave a strong FL emission peak between 670 and 739 nm in their FL spectra, respectively (Fig. 2b and Table 1). The data indicated that the electron density and configuration of the aza-BODIPYs significantly impacted the FL emission. Aza-BODIPYs **1a–1c** without electron-donating MeO groups had maximum FL emission peaks between 670 and 685 nm. In comparison, aza-BODIPYs **1d–1f** with MeO groups gave much red-shifted maximum FL emis-

sion peaks between 720 and 739 nm in the near-infrared (NIR) region with a Stokes shift up to 48 nm. Third, all the aza-BODIPYs except for **1e** gave a high molar extinction coefficient (ε) and FL quantum yield (ϕ_f, Table 1). The mismatched electron donor–acceptor configuration of aza-BODIPY **1e** may account for its low UV absorption, FL emission, molar extinction coefficient, FL quantum yield, and abnormal Stokes shift. The data suggested that forming a donor–acceptor electron configuration with MeO groups at the lower sphere and CF_3 groups at the upper sphere is preferred, promoting red-shifts in UV absorption and FL emission without significantly impacting the ε and ϕ_f values. In contrast, introducing CF_3 groups at the lower sphere may boost UV absorption and FL emission blue-shifts.

Next, the photothermal conversion capability of aza-BODIPYs **1a–1f** was investigated. Under irradiation with a 660 nm laser at 0.5 W cm^{-2} for 6 min, temperature changes (ΔT) of 11.3 to 22.1 °C were detected for aza-BODIPYs **1a–1f** (Fig. 3). Compared to many aza-BODIPY-based photothermal agents,[11] **1a–1f** showed moderate photothermal conversion capability. But, it is evident that the CF_3 groups significantly impact the photothermal conversion capability of the aza-BODIPYs. Consistent with the UV absorption and FL emission red-shift trends, aza-BODIPYs **1a** and **1d** with CF_3 groups at the upper sphere have a much higher photothermal conversion capability than their counterparts **1b** and **1e** with CF_3 groups at the lower sphere. Furthermore, introducing CF_3 groups into the aza-BODIPYs seems to hamper the photothermal conversion capability, with **1a** as an exception because **1b**, **1d**, and **1e** all show a much lower ΔT than their non-trifluoromethylated counterparts **1c** and **1f**.
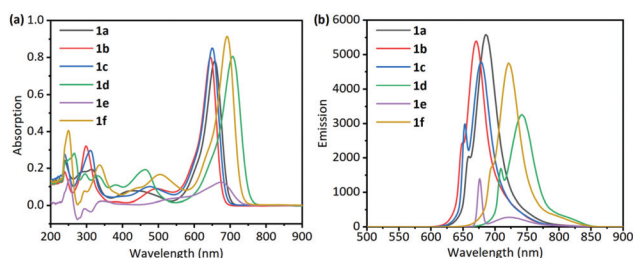
Fig. 2 (a) UV–Vis absorption spectra and (b) FL emission spectra of aza-BODIPYs **1a–1f** (10 μM in chloroform).
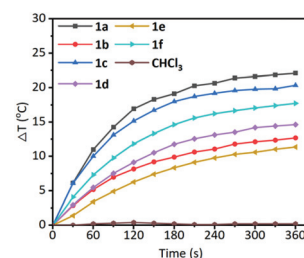
Fig. 3 Temperature changes of aza-BODIPYs **1a–1f** (20 μM) in CHCl$_3$ under irradiation with a 660 nm laser at 0.5 W cm^{-2} for 6 min.

Table 1 Photophysical properties of aza-BODIPYs **1a–1f** in chloroform

	$\lambda_{abs}{}^a$ (nm)	$\lambda_{Ex}{}^a$ (nm)	$\lambda_{Em}{}^a$ (nm)	Stokes shift (nm)	ε (M^{-1} cm^{-1})	ϕ_f	ϕ_Δ
1a	656	655	685	29	81 430	0.44[b]	0.05
1b	644	645	670	26	85 450	0.45[b]	0.69
1c	650 (650[d])	650	677 (672[d])	27 (22[d])	82 520 (79 000[d])	0.34[b,c,d]	0.07
1d	706	706	739	33	83 040	0.35[b]	0.02
1e	674	674	722	48	13 260	0.26[c]	0.24
1f	691	691	720	29	96 550	0.28[b]	0.04

^{a} Concentration : 10 μM. ^{b} Concentration: 0.2 μM. ^{c} Concentration: 2 μM. ^{d} Literature data are presented in the parentheses.[13]

The ROS generation ability of aza-BODIPYs **1a–1f** was measured using time-dependent UV-Vis absorption spectra, with DPBF as the ROS-sensitive UV-Vis probe using a 660 nm laser at 0.5 W cm^{-2}.[12] Laser irradiation of a DPBF chloroform solution alone caused negligible absorption intensity changes, which indicated no ROS generation from the control solution (see ESI Fig. S2†). In contrast, significant UV-Vis absorption intensity changes were detected from the aza-BODIPYs and DPBF solutions, showing that aza-BODIPYs **1a–1f** can efficiently generate ROS under laser irradiation (Fig. 4). However, their ROS generating abilities are quite different. Aza-BODIPY **1b** may be a powerful PDT agent, which generated ROS and consumed DPBF in the solution within 8 seconds under the conditions (Fig. 4b). In contrast, it took aza-BODIPY **1d** 4 min to consume DPBF under the same conditions (Fig. 4d). In order to quantitatively evaluate the ROS generation capability, the photochemical quantum yields (ϕ_Δ) for the $^1O_2$ generation of aza-BODIPYs **1a–1f** were measured (Table 1). The ϕ_Δ values showed the high $^1O_2$ generation capability of aza-BODIPYs **1b** and **1e** (**1b**: ϕ_Δ = 0.69, **1e**: ϕ_Δ = 0.24), which was consistent with the DPBF consumption time measurements. The data showed that CF$_3$ groups also play an essential role in the ROS generating capability of the aza-BODIPYs. Aza-BODIPYs **1b** and **1e** with CF$_3$ groups at the lower sphere exhibited a higher ROS generating ability and aza-BODIPYs **1a** and **1d** with CF$_3$ groups at the upper sphere showed a lower ROS generating ability,

which suggested that mismatched electron donor–acceptor configuration promotes ROS generation.

To better understand the optical properties of aza-BODIPYs **1a–1f**, density functional theory (DFT) at the B3LYP/6-31 G(d, P) level was employed to calculate their HOMO and LUMO energy levels (Fig. 5). For aza-BODIPYs **1a–1d** and **1f**, the calculated HOMO and LUMO were mainly localized in the aza-BODIPY cores and the lower sphere, while the HOMO of aza-BODIPY **1e** was mainly localized in the aza-BODIPY cores and upper sphere, which may be responsible for its abnormal optical and photodynamic properties. Furthermore, the introduction of CF$_3$ groups at the upper sphere promoted the electron donor–acceptor configuration and lowered the energy gap between the HOMO and LUMO, while the introduction of CF$_3$ groups at the lower sphere actually hampered the electron donor–acceptor configuration and slightly elevated the energy
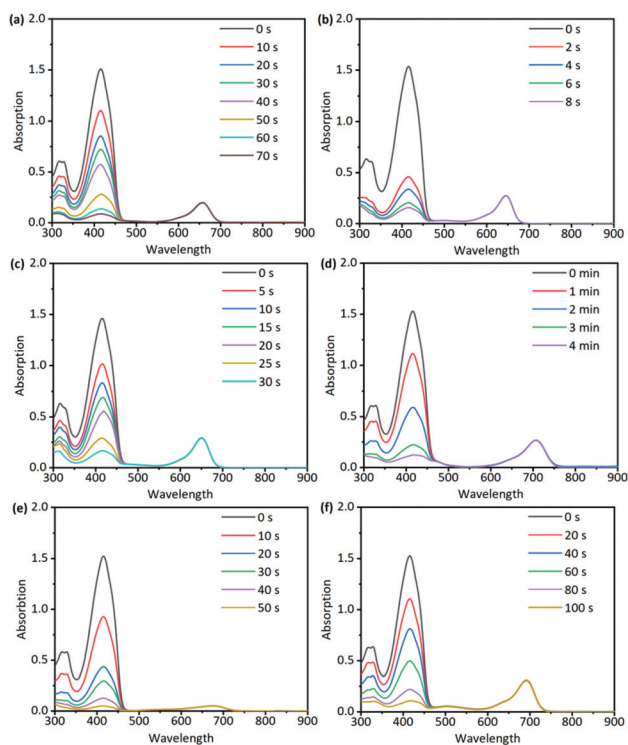
Fig. 4 The time-dependent UV-vis absorption spectra of DPBF (40 μM) and aza-BODIPYs (3 μM; a: **1a**, b: **1b**, c: **1c**, d: **1d**, e: **1e**, f: **1f**) solution in CHCl$_3$ under irradiation with a 660 nm laser at 0.5 W cm^{-2}.
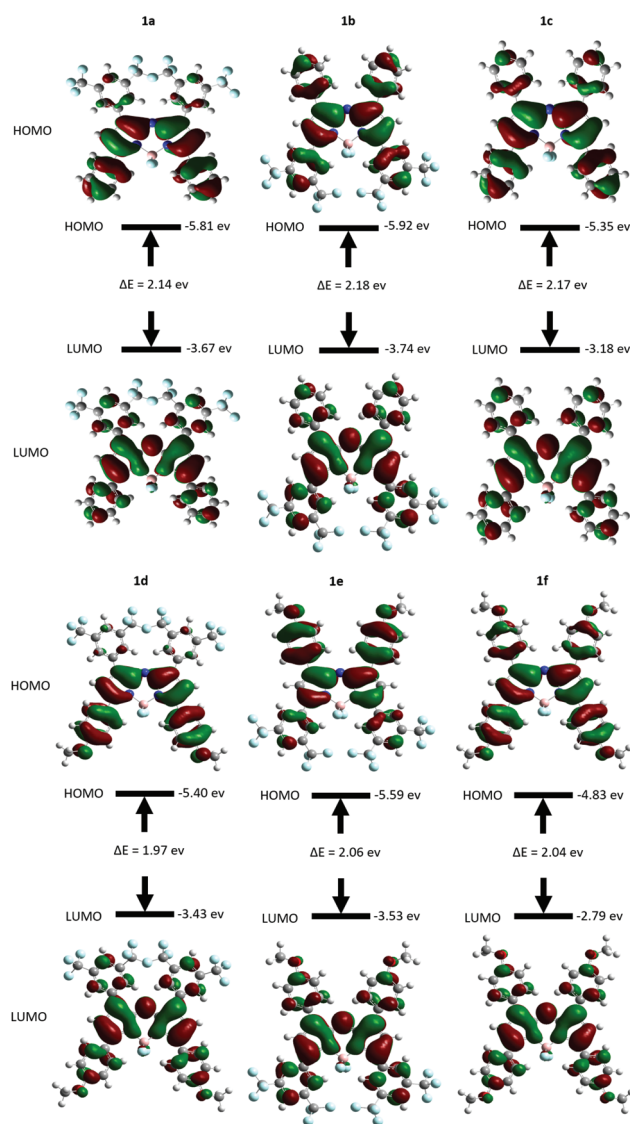
Fig. 5 Frontier molecular orbitals HOMO and LUMO of aza-BODIPYs **1a–1f** at the B3LYP/6-31 G(d, P) level with Gaussian 09.

This journal is © The Royal Society of Chemistry 2022

Org. Biomol. Chem., 2022, **20**, 3335–3341 | **3339**
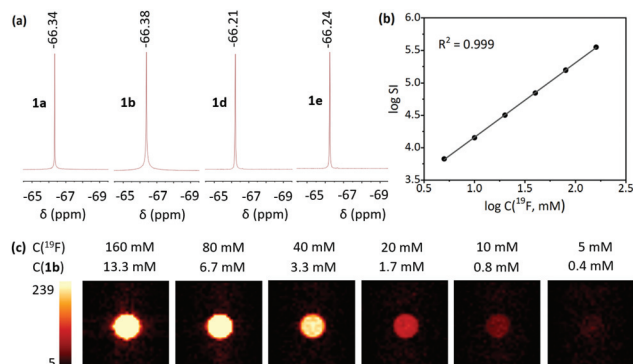
Fig. 6 (a) ^{19}F NMR of aza-BODIPYs (CDCl$_3$ as the solvent). (b) Plot of log SI *vs.* log $C(^{19}$F) and (c) ^{19}F MRI phantom images (chloroform with 10% CDCl$_3$ as the solvent) of **1b**.

gap between the HOMO and LUMO, which may promote the photochemical quantum yields for $^1O_2$ generation.

Finally, the ^{19}F NMR and ^{19}F MRI capability of the tetra-trifluoromethylated aza-BODIPYs was investigated. A strong and singlet ^{19}F NMR peak around −66.3 ppm from twelve symmetrical fluorines (Fig. 6a) facilitated the sensitive monitoring of aza-BODIPYs **1a**, **1b**, **1d**, and **1e** with ^{19}F NMR. Moreover, the strong and unified ^{19}F NMR peak makes the aza-BODIPYs sensitive ^{19}F MRI agents without chemical shift-induced imaging artifacts. Compared to aza-BODIPYs **1a**, **1d**, and **1e**, **1b** has the highest ROS generation ability, and a high molar extinction coefficient and FL quantum yield, and would be a promising FL-^{19}F MRI dual-imaging traceable PDT agent. Indeed, aza-BODIPY **1b** showed high ^{19}F MRI sensitivity in a phantom, concentration-dependent ^{19}F MRI experiment, where ^{19}F MRI was analysed at a concentration as low as 5 mM with a data collection time of 11 seconds (Fig. 6c). Furthermore, the ^{19}F MRI signal intensity is proportional to the ^{19}F concentration (Fig. 6b), which enables the accurate quantification of the ^{19}F MRI signal with the ^{19}F concentration.

Conclusions

In summary, we have developed a series of novel tetra-trifluoro-methylated aza-BODIPYs and identified one as a promising FL-^{19}F MRI dual-imaging traceable photosensitizer for PDT. The combinatory synthesis from commercially available building blocks facilitated rapid and convenient preparation of a library of aza-BODIPYs with diverse structures. From the side-by-side comparison, the role of CF$_3$ groups in optimizing the performance of aza-BODIPYs was disclosed: CF$_3$ groups at the upper sphere are preferred for the red-shift of UV-Vis absorption and FL emission. In contrast, CF$_3$ groups at the lower sphere promote ROS generation. However, the introduction of CF$_3$ groups usually reduces the photothermal conversion ability. Besides, the introduction of four CF$_3$ groups facilitates a strong and unified ^{19}F signal for the sensitive and quantitat-

ive monitoring of the aza-BODIPYs with "hot-spot" ^{19}F MRI. Notably, the sensitive chemical shift and relaxation times of ^{19}F NMR may provide bountiful *in vivo* information, such as the local oxygen concentration, molecular interactions, degradation, *etc.*, at a ^{19}F concentration much lower than that of ^{19}F MRI, which would be of great importance for optimizing PDT of cancer. The study not only provides a promising dual-imaging-traceable PDT agent, but also boosts the rational design of fluorinated aza-BODIPYs. The application of fluorinated aza-BODIPYs in developing novel theranostics for cancer is currently in progress and will be published in due course.

Conflicts of interest

The authors declare no conflicts of interest.

Acknowledgements

References

1 (*a*) X. Li, J. Kim, J. Yoon and X. Chen, *Adv. Mater.*, 2017, **29**, 1606857; (*b*) Y. Xia, M. V. Matham, H. Su, P. Padmanabhan and B. Gulyás, *J. Biomed. Nanotechnol.*, 2016, **12**, 1553–1584; (*c*) J. Rieffel, U. Chitgupi and J. F. Lovell, *Small*, 2015, **11**, 4445–4461; (*d*) S. Y. Lee, S. I. Jeon, S. Jung, I. J. Chung and C.-H. Ahn, *Adv. Drug Delivery Rev.*, 2014, **76**, 60–78; (*e*) D.-E. Lee, H. Koo, I.-C. Sun, J. H. Ryu, K. Kim and I. C. Kwon, *Chem. Soc. Rev.*, 2012, **41**, 2656–2672; (*f*) W.-Y. Huang and J. J. Davis, *Dalton Trans.*, 2011, **40**, 6087–6103; (*g*) A. Louie, *Chem. Rev.*, 2010, **110**, 3146–3195; (*h*) J. Kim, Y. Piao and T. Hyeon, *Chem. Soc. Rev.*, 2009, **38**, 372–390.

2 (*a*) C. Qi, J. Lin, L.-H. Fu and P. Huang, *Chem. Soc. Rev.*, 2018, **47**, 357–403; (*b*) X. Ai, J. Mu and B. Xing, *Theranostics*, 2016, **6**, 2439–2456; (*c*) W. Xie, Z. Guo, F. Gao, Q. Gao, D. Wang, B.-S. Liaw, Q. Cai, X. Sun, X. Wang and L. Zhao, *Theranostics*, 2018, **8**, 3284–3307; (*d*) Q. Dai, H. Geng, Q. Yu, J. Hao and J. Cui, *Theranostics*, 2019, **9**, 3170–3189; (*e*) X. Li, W. Li, M. Wang and Z. Liao, *J. Controlled Release*, 2021, **335**, 437–448; (*f*) M. Chen, D. Liu, F. Liu, Y. Wu, X. Peng and F. Song, *J. Controlled Release*, 2021, **332**, 269–284; (*g*) A. G. Robertson and L. M. Rendin, *Chem. Soc. Rev.*, 2021, **50**, 4231–4244.

3 (*a*) J. Ruiz-Cabello, B. P. Barnett, P. A. Bottomley and J. W. M. Bulte, *NMR Biomed.*, 2011, **24**, 114–129; (*b*) J. C. Knight, P. G. Edwards and S. J. Paisey, *RSC Adv.*, 2011, **1**, 1415–1425; (*c*) I. Tirotta, V. Dichiarante,

3340 | *Org. Biomol. Chem.*, 2022, **20**, 3335–3341

This journal is © The Royal Society of Chemistry 2022

C. Pigliacelli, G. Cavallo, G. Terraneo, F. B. Bombelli, P. Metrangolo and G. Resnati, *Chem. Rev.*, 2015, **115**, 1106–1129.

4 (*a*) S. Mizukami, R. Takikawa, F. Sugihara, M. Shirakawa and K. Kikuchi, *Angew. Chem., Int. Ed.*, 2009, **48**, 3641–3643; (*b*) B. E. Rolfe, I. Blakey, O. Squires, H. Peng, N. R. B. Boase, C. Alexander, P. G. Parsons, G. M. Boyle, A. K. Whittaker and K. J. Thurecht, *J. Am. Chem. Soc.*, 2014, **136**, 2413–2419; (*c*) S. Bo, C. Song, Y. Li, W. Yu, S. Chen, X. Zhou, Z. Yang, X. Zheng and Z.-X. Jiang, *J. Org. Chem.*, 2015, **80**, 6360–6366; (*d*) Y. Zhang, S. Bo, T. Feng, X. Qin, Y. Wan, S. Jiang, C. Li, J. Lin, T. Wang, X. Zhou, Z.-X. Jiang and P. Huang, *Adv. Mater.*, 2019, **31**, 1806444; (*e*) J. Zhu, Y. Xiao, H. Zhang, Y. Li, Y. Yuan, Z. Yang, S. Chen, X. Zheng, X. Zhou and Z.-X. Jiang, *Biomacromolecules*, 2019, **20**, 1281–1287; (*f*) J. M. Janjic, M. Srinivas, D. K. K. Kadayakkara and E. T. Ahrens, *J. Am. Chem. Soc.*, 2008, **130**, 2832–2841.

5 (*a*) Z. Shi, X. Han, W. Hu, H. Bai, B. Peng, L. Ji, Q. Fan, L. Li and W. Huang, *Chem. Soc. Rev.*, 2020, **49**, 7533–7567; (*b*) D. Chen, Z. Zhong, Q. Ma, J. Shao, W. Huang and X. Dong, *ACS Appl. Mater. Interfaces*, 2020, **12**, 26914–26925; (*c*) S. Shimizu, *Chem. Commun.*, 2019, **55**, 8722–8743.

6 (*a*) M. I. M. Espinoz, L. Sori, A. Pizzi, G. Terraneo, I. Moggio, E. Arias, G. Pozzi, S. Orlandi, V. Dichiarante, P. Metrangolo, M. Cavazzini and F. Bombelli, *Chem. – Eur. J.*, 2019, **25**, 9078–9087; (*b*) A. Savoldelli, Q. Meng, R. Paolesse, F. R. Fronczek, K. M. Smith and M. G. H. Vicente, *J. Org. Chem.*, 2018, **83**, 6498–6507; (*c*) L. Liu, Y. Yuan, Y. Yang, M. T. McMahon, S. Chen and X. Zhou, *Chem. Commun.*, 2019, **55**, 5851–5854;

(*d*) A. M. Huynh, A. Müller, S. M. Kessler, S. Henrikus, C. Hoffmann, A. K. Kiemer, A. Bücker and G. Jung, *ChemMedChem*, 2016, **11**, 1–9; (*e*) T. Wu, A. Li, K. Chen, X. Peng, J. Zhang, M. Jiang, S. Chen, X. Zheng, X. Zhou and Z.-X. Jiang, *Chem. Commun.*, 2021, **57**, 7743–7757.

7 (*a*) B. M. Johnson, Y.-Z. Shu, X. Zhuo and N. A. Meanwell, *J. Med. Chem.*, 2020, **63**, 6315–6386; (*b*) E. P. Gillis, K. J. Eastman, M. D. Hill, D. J. Donnelly and N. A. Meanwell, *J. Med. Chem.*, 2015, **58**, 8315–8359; (*c*) R. Filler and R. Saha, *Future Med. Chem.*, 2009, **1**, 777–791; (*d*) S. P. Gupta, *Lett. Drug Des. Discovery*, 2019, **16**, 1089–1109; (*e*) A. A. Berger, J.-S. Völler, N. Budisa and B. Koksch, *Acc. Chem. Res.*, 2017, **50**, 2093–2103.

8 (*a*) J. R. Schmink, J. L. Holcomb and N. E. Leadbeater, *Org. Lett.*, 2009, **11**, 365–368; (*b*) A. Lator, S. Gaillard, A. Poater and J.-L. Renaud, *Chem. – Eur. J.*, 2018, **24**, 5770–5774.

9 R. Gresser, H. Hartmann, M. Wrackmeyer, K. Leo and M. Riede, *Tetrahedron*, 2011, **67**, 7148–7155.

10 W. Sheng, Y. Q. Zheng, Q. Wu, Y. Wu, C. Yu, L. Jiao, E. Hao, J. Y. Wang and J. Pei, *Org. Lett.*, 2017, **19**, 2893–2896.

11 (*a*) M. Zhao, Q. Zeng, X. Li, D. Xing and D. Zhang, *Nano Res.*, 2022, **15**, 716–727; (*b*) D. Chen, Z. Zhong, Q. Ma, J. Shao, W. Huang and X. Dong, *ACS Appl. Mater. Interfaces*, 2020, **12**, 26914–26925.

12 (*a*) Z. Yu, J. Zhou, X. Ji, G. Lin, S. Xu, X. Dong and W. Zhao, *J. Med. Chem.*, 2020, **63**, 9950–9964; (*b*) X. Jianga, T. Zhang, C. Sun, Y. Men and L. Xiao, *Chin. Chem. Lett.*, 2019, **30**, 1055–1058.

13 J. Killoran, L. Allen, J. F. Gallagher, W. M. Gallagher, D. F. O'Shea, *Chem. Commun.*, 2002, 1862–1863.

This journal is © The Royal Society of Chemistry 2022

Org. Biomol. Chem., 2022, **20**, 3335–3341 | **3341**